



Ionospheric VTEC and satellite DCB estimated from single-frequency BDS observations with multi-layer mapping function

Ke Su^{1,2} · Shuanggen Jin^{1,3,4} · J. Jiang³ · Mainul Hoque⁵ · Liangliang Yuan^{1,2}

Received: 8 October 2020 / Accepted: 29 January 2021 / Published online: 1 March 2021
© The Author(s), under exclusive licence to Springer-Verlag GmbH, DE part of Springer Nature 2021

Abstract

The ionospheric delays and satellite differential code biases (DCBs) act as the significant error sources in the global navigation satellite system (GNSS) positioning, navigation and timing (PNT) services, and are still challenging to estimate correctly. In this study, the ionospheric vertical total electron content (VTEC) and satellite DCBs are estimated by a refining single-frequency precise point positioning (SFPPP) method based on the multi-layer ionosphere mapping function (MF), as well as the dual-frequency methods, including the carrier-to-code leveling (CCL) and dual-frequency PPP (DFPPP). The solutions isolate the ionospheric VTEC values from the slant ionospheric delay with the generalized trigonometric series function (GTSF) and precisely estimate the satellite DCB with a zero-mean condition. The SFPPP-derived VTEC estimates are validated and evaluated by comparing with the International GNSS Service (IGS) products and using ionosphere-corrected (IC) SFPPP in both static and kinematic scenarios. Using the 74 experimental stations collected from the multi-GNSS experiment (MGEX) network from January to March 2020, the results show that the VTEC estimation precision by applying the multi-layer MF is improved for the SFPPP approach. The positioning performances of the static and kinematic BDS IC SFPPP with the ionospheric correction derived from the multi-layer MF SFPPP are better when compared to the single-layer MF. The estimated BDS DCB with the SFPPP is stable and of high accuracy. The SFPPP approach with multi-layer MF is demonstrated as a promising and reliable method to retrieve the VTEC and satellite DCB with the low-cost property for the GNSS users.

Keywords BeiDou Navigation Satellite System (BDS) · Vertical total electron content (VTEC) · Single-frequency · Precise point positioning (PPP) · Differential code bias (DCB)

Introduction

The ionospheric delay is an important error source for the single-frequency global navigation satellite system (GNSS) raw pseudorange and carrier phase measurements, which can cause range errors of more than 100 m (Hoque and Jakowski 2012). Since the ionosphere is a dispersive medium, the ionospheric delay can be eliminated by combining observations of two or more frequencies. For single-frequency GNSS users, however, it requires external ionospheric information to mitigate the delays. Two common ways are generally applied for ionospheric correction. One way is to directly employ external empirical ionospheric models, such as the Klobuchar model, NeQuick model, BeiDou Global Ionospheric delay correction Model (BDGIM) and Neustrelitz TEC model (NTCM) (Hoque and Jakowski 2015; Klobuchar 1987; Nava et al. 2008; Yuan et al. 2019). Another alternative method is to use the ionospheric total electron content

✉ Shuanggen Jin
sgjin@shao.ac.cn; sg.jin@yahoo.com

¹ Shanghai Astronomical Observatory, Chinese Academy of Sciences, Shanghai 200030, China

² University of Chinese Academy of Sciences, Beijing 100049, China

³ School of Remote Sensing and Geomatics Engineering, Nanjing University of Information Science and Technology, Nanjing 210044, China

⁴ Jiangsu Engineering Center for Collaborative Navigation/Positioning and Smart Applications, Nanjing 210044, China

⁵ Institute for Solar-Terrestrial Physics, German Aerospace Center, 17235 Neustrelitz, Germany

(TEC) map reconstructed from the stationary GNSS stations. The differential code bias (DCB), known as the hardware delay effects differences between the signals of different frequencies, is error in the ionospheric TEC estimates and in GNSS positioning, navigation and timing (PNT). Hence, the urgent need for ionospheric TEC and DCB estimates is justified for GNSS users.

In a quick succession of successful applications of the Global Positioning System (GPS), GLONASS, Galileo system and regional systems, including QZSS and IRNSS, the BeiDou Navigation Satellite System (BDS) fulfilled the constellation deployment goals with the successful launch of the last global networking satellite on June 23, 2020 (<http://www.beidou.gov.cn/>). The new BDS with global coverage has widely expanded the service areas and can provide short message communication, augmentation service capabilities and PNT services (Jin and Su 2020). Until now, the sufficient number of BDS satellites can be observed by the international GNSS service (IGS) multi-GNSS experiment (MGEX) network stations, which makes it possible to precisely estimate the ionospheric TEC and satellite DCB with the BDS observations.

Usually, the methods to estimate the ionospheric TEC and satellite DCB include the carrier-to-code leveling (CCL) and precise point positioning (PPP) (Liu et al. 2020; Psychas et al. 2018). The CCL, with the effectiveness and simplicity, is widely applied for retrieving the slant TEC by the dual-frequency measurements, whose accuracy is susceptible and sensitive to the leveling errors, multipath effects and receiver DCB intraday variation (Chen et al. 2018; Ciruolo et al. 2007). Much work has been done to overcome the shortcoming of the CCL and attain more reliable TEC retrieval. Zhang et al. (2012) proposed a method to extract the slant TEC by the GPS undifferenced and uncombined dual-frequency PPP (DFPPP), showing that the observational noise and multipath of the slant TEC is considerably reduced for more than 70% compared with values from the CCL. Tu et al. (2013) estimated and monitored the vertical TEC (VTEC) and satellite DCB with the real-time DFPPP, revealing that the real-time VTEC and satellite DCB have a bias of 1–2 TEC unit (TECU) and 0.4 ns compared with the IGS final products. The DFPPP approach has been widely applied to the applications of the ionospheric community (Li et al. 2020; Liu et al. 2018; Ren et al. 2016).

Comparing with the dual-frequency approaches, the retrieval of VTEC and satellite DCB with the single-frequency observations is more challenging in terms of the low-cost property. Schüller and Oladipo (2014) demonstrated that the code-minus-carrier (CMC) combination method with the single-frequency pseudorange and carrier phase observations can model the ionospheric VTEC or the high- and midlatitudes stations, whereas the VTEC estimate precision is highly affected by the multipath and pseudorange noises.

Alternatively, Zhang et al. (2018) jointly estimated the VTEC and satellite DCBs with high reliability and accuracy using the single-frequency PPP (SFPPP) approach. Li et al. (2019a) applied the SFPPP method to retrieve ionospheric VTEC with the BDS2 B1I data.

For all the above literatures, the corresponding mapping functions (MFs) in the ionospheric TEC modeling are based on the Earth's ionosphere single-layer assumption. However, the single-layer MF is likely to cause the more than 10 m ranges in the vertical direction owing to the strong horizontal gradients of the ionospheric ionization and strong deviations under ionospheric equilibrium conditions (Komjathy et al. 2005). Moreover, the ionospheric height of the single-layer MF significantly affects the mapping errors (Li et al. 2018; Xiang and Gao 2019). One option to improve the TEC mapping is to estimate the ionospheric 3-D electron density by the tomographic methods using the datasets collected from the dense data network with quantities of space- and ground-based receivers (Hernández-Pajares et al. 2005). In many cases, the relatively limited number of the ground-based receivers cannot satisfy the application of the tomographic methods. Another method is to divide the ionosphere into many spherical layers implemented with specific MFs (Li et al. 2019b). The two-layer approximation for modeling the ionospheric electron density variation was commonly applied for the regional or global areas with a high-spatial-resolution dataset. Consequently, the above two approaches are both applicable only when sufficient data coverage is available. Hoque and Jakowski (2013) proposed a multi-layer MF according to the ionospheric typical vertical structure described by the Chapman layer, revealing that mapping error can be reduced by more than 50% compared with single-layer MF.

This work aims to retrieve the ionospheric VTEC and satellite DCB with the BDS SFPPP solution. The multi-layer MF is applied to reduce mapping errors. Besides, the CCL and DFPPP approaches implemented with the single-layer and multi-layer MFs are also conducted and compared. The structure of this study is organized as follows. First, we address the BDS general pseudorange and carrier phase observations. Then, the methodologies of the CCL, SFPPP and DFPPP approaches and ionospheric VTEC modeling and satellite DCB determination with the single-layer and multi-layer MFs are presented. After introducing the processing strategies and the experimental data, we assessed the VTEC estimates by comparing with the IGS products and utilizing the ionosphere-corrected (IC) SFPPP approach. The stability and accuracy of the BDS satellite and receiver DCB are analyzed. Finally, conclusions are given.

Methodology

The BDS pseudorange and carrier phase observables are first presented. Then, the methods of CCL, SFPPP, DFPPP and ionospheric VTEC modeling are introduced.

General observation equations

The pseudorange and carrier phase observations for the specific BDS satellite s and receiver r pair at epoch k can be written as (Leick et al. 2015):

$$\begin{cases} p_{r,j}^s(k) = \rho_r^s(k) + dt_r(k) - dt^s(k) + T_r^s(k) + \mu_j \cdot I_{r,1}^s(k) + d_{r,j} - d_j^s + \epsilon_p(k) \\ \phi_{r,j}^s(k) = \rho_r^s(k) + dt_r(k) - dt^s(k) + T_r^s(k) - \mu_j \cdot I_{r,1}^s(k) + b_{r,j} - b_j^s + N_{r,j}^s(k) + \epsilon_\phi(k) \\ \mu_j = f_1^2 / f_j^2 \end{cases} \tag{1}$$

where $p_{r,j}^s(k)$ and $\phi_{r,j}^s(k)$ denote the pseudorange and carrier phase observations, $\rho_r^s(k)$ is the receiver and satellite geometrical range, and $dt_r(k)$ and $dt^s(k)$ are the receiver and satellite clock offsets from the GNSS system time. $T_r^s(k)$ denotes the tropospheric delay, $I_{r,1}^s(k)$ is the slant ionospheric delay on the BDS first frequency, μ_j denotes the frequency-dependent multiplier factor and f_j is j th frequency. $d_{r,j}$ and d_j^s denote the receiver and satellite pseudorange instrumental

Ionospheric observables extraction from CCL

When constructing geometry-free (GF) observations using BDS B1I/B3I measurements, the respective equations read (Zhang et al. 2019):

$$\begin{cases} p_{r,GF}^s(k) = \mu_{GF} \cdot I_{r,1}^s(k) + d_{r,GF} - d_{,GF}^s + \epsilon_{p,GF}(k) \\ \phi_{r,GF}^s(k) = -\mu_{GF} \cdot I_{r,1}^s(k) + b_{r,GF} - b_{,GF}^s + N_{r,GF}^s(k) + \epsilon_{\phi,GF}(k) \end{cases} \tag{2}$$

where operation $(\cdot)_{GF} = (\cdot)_1 - (\cdot)_2$ denotes the GF combination creation, and $\epsilon_{p,GF}$ and $\epsilon_{\phi,GF}$ denote the pseudorange and carrier phase GF measurement noise. Note $d_{r,GF}$ and $d_{,GF}^s$

also denote the B1I/B3I receiver and satellite differential code bias (DCB), respectively.

The pseudorange DCB can be viewed as constant in a day or few hours (Gao et al. 2017). It can also be considered as constant for the carrier phase ambiguities in a continuous arc without the cycle slip occurring. Using the average values of the pseudorange and carrier phase over one arc of data with no cycle slips, we can write the equations as:

$$\begin{aligned} \frac{1}{n} \sum_{k=1}^n [p_{r,GF}^s(k) + \phi_{r,GF}^s(k)] &= \frac{1}{n} \sum_{k=1}^n [d_{r,GF}] - \frac{1}{n} \sum_{k=1}^n [d_{,GF}^s] + \frac{1}{n} \sum_{k=1}^n [b_{r,GF}] - \frac{1}{n} \sum_{k=1}^n [b_{,GF}^s] + \frac{1}{n} \sum_{k=1}^n [N_{r,GF}^s(k)] \\ &= d_{r,GF} - d_{,GF}^s + b_{r,GF} - b_{,GF}^s + N_{r,GF}^s \end{aligned} \tag{3}$$

where symbol $\frac{1}{n} \sum_{k=1}^n [\]$ denotes the averaging operation.

Applying (3) to the GF carrier phase observables in (2), the smooth ionospheric observables can be written as:

$$-\mu_{GF}^{-1} \cdot \left\{ \phi_{r,GF}^s(k) - \frac{1}{n} \sum_{k=1}^n [p_{r,GF}^s(k) + \phi_{r,GF}^s(k)] \right\} = I_{r,1}^s(k) - \mu_{GF}^{-1} \cdot d_{,GF}^s + \mu_{GF}^{-1} \cdot d_{r,GF} + \epsilon'_{\phi}(k) \tag{4}$$

delays, $b_{r,j}$ and b_j^s denote the carrier phase hardware delays, $N_{r,j}^s(k)$ is the integer ambiguity. Finally, ϵ_p and ϵ_ϕ denote the pseudorange and carrier phase measurement noise with variances of σ_p^2 and σ_ϕ^2 , including multipath. Note that the epoch k index does not exist in the assumed time-constant parameters.

The solvable ionospheric estimate in the CCL method combines the slant ionospheric delay, receiver and satellite DCB. With the n epochs continuous arc, the variance of the smooth ionospheric observables can be written as:

$$\sigma_{GF,S}^2 = \frac{1}{n} \sigma_{p,GF}^2 + \frac{n+1}{n} \sigma_{\phi,GF}^2 = \frac{2}{n} \sigma_p^2 + \frac{2n+2}{n} \sigma_\phi^2 \tag{5}$$

where $\sigma_{GF,S}^2$ denotes the smooth ionospheric observables variance.

Ionospheric observables extraction from SFPPP

Conventionally, the precise satellite clock products estimated with ionosphere-free observations are biased by the ionosphere-free combination of the satellite instrument code delay, which reads (Sterle et al. 2015),

$$d\hat{t}^s(k) = dt^s(k) + d_{,IF}^s \tag{6}$$

where operation $(\cdot)_{IF} = J \cdot [(\cdot)_1 (\cdot)_2]^T = -\frac{1}{\mu_{GF}} [\mu_2 -1] \cdot [(\cdot)_1 (\cdot)_2]^T$ denotes creating the ionosphere-free combination.

The ionospheric delay can be parameterized and estimated as the unknowns, leading to the ionosphere-float (IF) model. With the prior known satellite position and clock and receiver position, the observation equations of IF SFPPP can be expressed as:

$$\begin{cases} \bar{p}_{r,j}^s(k) = m_r^s(k) \cdot ZWD_r(k) + d\hat{t}_r(k) + \mu_j \cdot \hat{I}_{r,1}^s(k) + \varepsilon_p(k) \\ \bar{\phi}_{r,j}^s(k) = m_r^s(k) \cdot ZWD_r(k) + d\hat{t}_r(k) - \mu_j \cdot \hat{I}_{r,1}^s(k) + \hat{N}_{r,j}^s(k) + \varepsilon_\phi(k) \end{cases} \tag{7}$$

with

$$\begin{cases} d\hat{t}_r(k) = dt_r(k) + d_{r,j} \\ \hat{I}_{r,1}^s(k) = I_{r,1}^s(k) - \mu_{GF}^{-1} \cdot d_{,GF}^s \\ \hat{N}_{r,j}^s(k) = N_{r,j}^s(k) + b_{r,j} - b_j^s - d_{r,1} - \mu_j \cdot \mu_{GF}^{-1} \cdot d_{,GF}^s + d_{,IF}^s \end{cases} \tag{8}$$

where $\bar{p}_{r,j}^s(k)$ and $\bar{\phi}_{r,j}^s(k)$ denote the observed-minus-calculated (OMC) pseudorange and carrier phase observations. $m_r^s(k)$ denotes the tropospheric wet mapping function. $ZWD_r(k)$ denotes the tropospheric zenith wet delay (ZWD). Identifiers with ^ denote the re-parameterized parameters.

Since the SFPPP mentioned above model have one size rank deficiency, the receiver clock is re-parameterized as the

$$\begin{cases} d\bar{t}_r(k) = dt_r(k) + d_{r,IF} \\ \bar{I}_{r,1}^s(k) = I_{r,1}^s(k) - \mu_{GF}^{-1} \cdot d_{,GF}^s + \mu_{GF}^{-1} \cdot d_{r,GF} \\ \hat{N}_{r,1}^s(k) = N_{r,1}^s(k) + b_{r,1} - b_{,1}^s - d_{r,IF} + \mu_{GF}^{-1} \cdot d_{r,GF} - \mu_{GF}^{-1} \cdot d_{,GF}^s \\ \hat{N}_{r,2}^s(k) = N_{r,2}^s(k) + b_{r,2} - b_{,2}^s - d_{r,IF} + \mu_2 \cdot \mu_{GF}^{-1} \cdot d_{r,GF} - \mu_2 \cdot \mu_{GF}^{-1} \cdot d_{,GF}^s \end{cases} \tag{12}$$

changes of values relative to the first epoch to acquire the full-rank observation equations, which can be expressed as:

$$\begin{cases} d\bar{t}_r(k) = d\hat{t}_r(k) - d\hat{t}_r(1) \\ \bar{I}_{r,1}^s(k) = \hat{I}_{r,1}^s(k) + d\hat{t}_r(1)/\mu_j \\ \bar{N}_{r,j}^s(k) = \hat{N}_{r,j}^s(k) + 2d\hat{t}_r(1) \end{cases} \tag{9}$$

where $d\bar{t}_r(k)$, $\bar{I}_{r,1}^s(k)$ and $\bar{N}_{r,j}^s(k)$ denote the estimable receiver clock, slant ionospheric delay and carrier phase ambiguity parameters.

Hence, we can express the full-rank design matrix $B_{r,j}(k)$ and estimable parameters $X(k)$ in the IF SFPPP model with n satellites and the j th frequency signal as:

$$\begin{cases} B_{r,j}(k) = \begin{bmatrix} e_2 \otimes \begin{pmatrix} m_r^1(k) \\ \dots \\ m_r^n(k) \end{pmatrix} e_2 \otimes e_n \begin{pmatrix} \mu_j \\ -\mu_j \end{pmatrix} \otimes I_n \begin{pmatrix} 0 \\ 1 \end{pmatrix} \otimes I_n \end{bmatrix} \\ X(k) = \begin{bmatrix} ZWD_r(k) & d\bar{t}_r(k) & \bar{I}_{r,1}^s(k) & \dots & \bar{I}_{r,1}^s(k) & \bar{N}_{r,j}^s(k) & \dots & \bar{N}_{r,j}^s(k) \end{bmatrix} \end{cases} \tag{10}$$

where e_n denotes the n -row vector in which all values are 1. I_n denotes the n -dimensional identity matrix. \otimes denotes the Kronecker product operation.

Ionospheric observables extraction from DFPPP

The equations of the BDS pseudorange and carrier phase observations in BDS IF DFPPP model can be written as:

$$\begin{cases} \bar{p}_{r,1}^s(k) = m_r^s(k) \cdot ZWD_r(k) + d\bar{t}_r(k) + \bar{I}_{r,1}^s(k) + \varepsilon_p(k) \\ \bar{p}_{r,2}^s(k) = m_r^s(k) \cdot ZWD_r(k) + d\bar{t}_r(k) + \mu_2 \cdot \bar{I}_{r,1}^s(k) + \varepsilon_p(k) \\ \bar{\phi}_{r,1}^s(k) = m_r^s(k) \cdot ZWD_r(k) + d\bar{t}_r(k) - \bar{I}_{r,1}^s(k) + \hat{N}_{r,1}^s(k) + \varepsilon_\phi(k) \\ \bar{\phi}_{r,2}^s(k) = m_r^s(k) \cdot ZWD_r(k) + d\bar{t}_r(k) - \mu_2 \cdot \bar{I}_{r,1}^s(k) + \hat{N}_{r,2}^s(k) + \varepsilon_\phi(k) \end{cases} \tag{11}$$

with

Similarly, the full-rank design matrix and estimable parameters in DFPPP model can be written as:

$$\begin{cases} B_r(k) = \begin{bmatrix} e_4 \otimes \begin{pmatrix} m_r^1(k) \\ \dots \\ m_r^n(k) \end{pmatrix} e_4 \otimes e_n \begin{pmatrix} 1 \\ -1 \\ \mu_2 \\ -\mu_2 \end{pmatrix} \otimes I_n \begin{pmatrix} 0 \\ 1 \end{pmatrix} \otimes I_2 \otimes I_n \end{bmatrix} \\ X(k) = \begin{bmatrix} ZWD_r(k) & d\bar{t}_r(k) & \bar{I}_{r,1}^s(k) & \dots & \bar{I}_{r,1}^s(k) & \bar{N}_{r,1}^s(k) & \dots & \bar{N}_{r,1}^s(k) & \bar{N}_{r,2}^s(k) & \dots & \bar{N}_{r,2}^s(k) \end{bmatrix} \end{cases} \tag{13}$$

where $B_r(k)$ and $X(k)$ denote the design matrix and estimated parameters.

Ionospheric TEC modeling

As described above, the PPP- or CCL-derived slant ionospheric delays are biased by satellite and receiver hardware delays. The unified forms of the estimable slant ionospheric delays from the CCL, SFPPP and DFPPP solutions read:

$$\bar{I}_{r,1}^s(k) = I_{r,1}^s(k) - \mu_{GF}^{-1} \cdot d_{,GF}^s + \Delta + \varepsilon_r(k) \tag{14}$$

with

$$\Delta = \begin{cases} \mu_{GF}^{-1} \cdot d_{r,GF}, & \text{CCL;DFPPP} \\ d\hat{t}_r(1)/\mu_j, & \text{SFPPP} \end{cases} \tag{15}$$

The DFPPP-derived slant ionospheric delays have an identical form with their counterparts obtained from CCL. The difference for the expressions is that the third parameter in CCL or DFPPP is linearly dependent on the receiver DCB, whereas the corresponding value in SFPPP encompasses only the receiver clock offsets on the first epoch.

The unbiased slant ionosphere delay can be expressed as the linear relation of the relatively accurate slant TEC (STEC) value $STEC_r^s(k)$, which reads (dos Santos Prol et al. 2018):

$$I_{r,1}^s(k) = \frac{A}{f_1^2} \cdot STEC_r^s(k) = \frac{40.28}{f_1^2} \cdot STEC_r^s(k) \tag{16}$$

The link of the STEC and VTEC can be computed with a so-called obliquity factor, which is normally known as the ionosphere MF that depends on the satellite elevation. Assuming that the ionosphere shell height is fixed at a certain value, a single-layer MF can be established, which can be written as (Jiang et al. 2018):

$$MF(E) = \frac{STEC_r^s(k)}{VTEC_r(k)} = \left[1 - \left(\frac{R_E \cdot \sin \left[\gamma \left(\frac{\pi}{2} - E \right) \right]}{R_E + H_{ion}} \right)^2 \right]^{-1/2} \tag{17}$$

where E denotes the elevation. $VTEC_r(k)$ denotes the VTEC. $R_E = 6371$ km denotes the mean earth radius. H_{ion} denotes the height of the assumed single layer and is set as 450 km since the Center for Orbit Determination in Europe (CODE) TEC maps used are optimized for this height. γ denotes the model coefficient, which is 1 for the single-layer MF (SLM) model and 0.9782 for the modified SLM (MSLM) model (Brunini and Azpilicueta 2010).

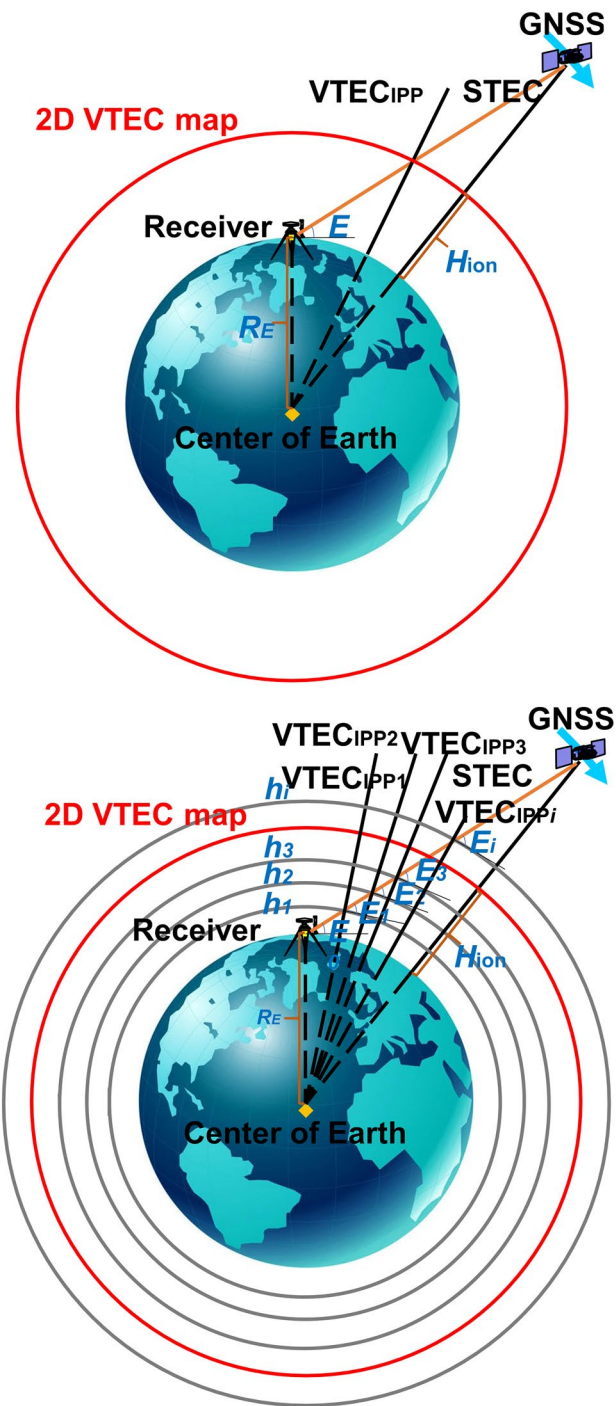


Fig. 1 Sketch map of the single-layer (top) and multi-layer (bottom) MFs

In a multi-layer MF approach, instead of collapsing the ionospheric vertical structure into a thin shell, the ionosphere is considered composed of numerous thin shells. A Chapman profile models the vertical structure (Rishbeth and Garriott 1969). The slant path intersects each ionospheric shell of incremental thickness with the height of $h_1, h_2, h_3,$

... and h_n . The corresponding intersection points projected at the two-dimensional thin-shell surfaces, which are called VTEC1, VTEC2, VTEC3, ... and VTEC n , respectively. Hence, the horizontal ionization gradients are included in the multi-layer MF. Similar to single-layer MF, the ionospheric pierce point (IPP) single-layer height can also be set to 450 km according to the current investigation (Kong et al. 2016). The incremental STEC, i.e., STEC $_1^2$, STEC $_2^3$, STEC $_3^4$, ... and STEC $_n^{n+1}$, can be acquired by the corresponding VTEC and obliquity factors determined from the Chapman layer function, which can be expressed as (Hoque and Jakowski 2013):

$$MF(E_i) = \frac{STEC_i^{i+1}}{VTEC_i} \approx \left[1 - \left(\frac{(R_E + h_i) \cdot \sin \left[\gamma \left(\frac{\pi}{2} - E_i \right) \right]}{R_E + h_{mIPP_i}} \right)^2 \right]^{-1/2} \cdot \left[\operatorname{erf} \left(- \frac{\exp \left(- \frac{h_i - h_{mIPP_i}}{H_{mIPP_i}} \right)}{\sqrt{2}} \right) \right]_{h_i}^{h_{i+1}} \quad (18)$$

where h_{mIPP_i} denotes the peak ionization height and H_{mIPP_i} denotes the atmospheric scale height. The two parameters are kept constant at 350 km and 70 km as fixed parameters, or acquired from supplementary measurements or empirical models. The single-layer and multi-layer MF sketch map is shown in Fig. 1.

For single-station-based ionospheric VTEC modeling, the generalized trigonometric series function (GTSF) is usually used to isolate the absolute ionospheric TEC value, in which the VTEC at the IPP is modeled as a function of time and geographical location and can be described as (Li et al. 2015):

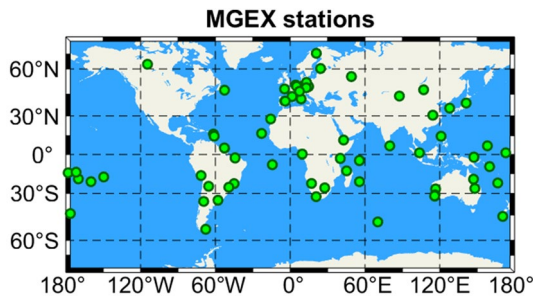


Fig. 2 Distribution of the selected MGEX data

$$VTEC_r(\varphi, T) = \sum_{n=0}^2 \sum_{m=0}^2 \{ E_{nm} \cdot (\varphi - \varphi_0)^n \cdot T^m \} + \sum_{k=0}^4 \{ C_k \cdot \cos(k \cdot T) + S_k \cdot \sin(k \cdot T) \} \quad (19)$$

with

$$T = \frac{2\pi \cdot (t - 14)}{24} \quad (20)$$

Table 1 Receiver and antenna types of the selected 74 MGEX stations

Stations	Receiver types	Antenna types
MIZU, OUS2, UNSA	SEPT ASTERX4	SEPCHOKE_B3E6
ABMF, REUN, NRMG	SEPT POLARX5	TRM57971.00
AREG, DJIG, PTGG, NKLK, HARB, TLSG		TRM59800.00
AJAC,		TRM115000.00
TOW2, KOUG, THTG		LEIAR25.R3
FAA1, GAMG, STJ3		LEIAR25.R4
CEBR, GOP6, KOUR, REDU, KIRU, VILL, NNOR, MAL2, MAS1, MGUE, YEL2		SEPCHOKE_B3E6
BRUX, POHN		JAVRINGANT_DM
BRST, LMMF	TRIMBLE ALLOY	TRM57971.00
KRGG		LEIAR25.R4
KZN2, MCHL, RGDG		TRM59800.00
ASCG, CHPG, CVPG, CUT0, FTNA, JFNG, KIRI, MAYG, METG, MRO1, NIUM, OWMG, PERT, PNGM, SEYG, TLSE, UFPR, ZIM2, ZIM3	TRIMBLE NETR9	TRM59800.00
CKIS, SAMO, SOLO		JAVRINGANT_DM
SALU		TRM115000.00
SIN1		LEIAR25.R3
LPGS, NYA2, POTS, SGOE, SUTM, ULAB, URUM, WIND, WUH2	JAVAD TRE_3	JAVRINGANT_G5T
FFMJ, WTZZ	JAVAD TRE_3 DELTA	LEIAR25.R3
HUEG		LEIAR25.R4

Table 2 Processing strategies of the ionospheric TEC and satellite DCB retrieval

Item	Processing strategies
<i>Part I: Slant ionospheric delay extraction: (CCL & PPP)</i>	
Observations	BDS: B1I/B3I
Weight schemes	Elevation weight; a prior precision of the 0.004 m and 0.4 m are set, respectively, for the BDS MEO/IGSO carrier phase and pseudorange observations. The BDS MEO/IGSO and GEO observation weighting ratio is 10:1 (Su and Jin 2019)
Estimator	PPP: Forward and backward Kalman filter
Sampling rate	30 s
Elevation cutoff	7°
Satellite orbit and clock	Fixed by Deutsches GeoForschungsZentrum (GFZ) precise orbit and clock products
Satellite DCB	PPP: absorbed by slant ionospheric delay
Earth rotation	PPP: fixed by the model (Petit and Luzum 2010)
Relativistic effect	PPP: fixed by the model (Kouba 2009)
Phase windup effect	PPP: fixed by the model (Wu et al. 1992)
Tide effect	PPP: Solid Earth, pole and ocean tide (Petit and Luzum 2010)
Satellite and receiver antenna offset	PPP: fixed by MGEX values
Receiver position	PPP: fix by IGS values
Receiver clock	PPP: estimated as white noises (10 ⁵ m ² /s)
Tropospheric delay	PPP: VMF3/GPT3/Modified Hopfield for tropospheric dry delay and estimated for tropospheric zenith wet delay (ZWD) by VMF3 as random walk processing (10 ⁻⁹ m ² /s) (Landskron and Böhm 2018; Su and Jin 2018)
Slant ionospheric delay	PPP: estimated as white noise process (10 ⁴ m ² /s) (Su et al. 2019)
Carrier phase ambiguity	PPP: estimated as constants
<i>Part II: Ionospheric TEC and satellite DCB retrieval</i>	
Estimator	Least square (LS) method
Estimated DCB type	BDS: C2I-C6I
Slant ionospheric delay	Acquired from CCL, SFPPP and DFPPP
DCB datum	Zero-mean condition (Jin et al. 2012)
Ionospheric TEC modeling function	GTSF (Li et al. 2015)
Ionospheric MFs	1. Single-layer MF (MSLM) 2. Multi-layer MF: Peak height hmF2 values derived from the Neustrelitz Peak Height Model (NPHM) (Hoque and Jakowski 2012); Scale height values derived from Neustrelitz TEC Model (NTCM) and Neustrelitz Peak Density Model (NPDM) via Chapman layer assumption and slab thickness estimation (Hoque and Jakowski 2011; Jakowski et al. 2011; Yuan et al. 2020).

where φ and φ_0 denote the geographical latitude for IPP and receiver, respectively. T denotes the function of local time t at IPP. E_{nm} , C_k and S_k denote the estimated coefficients in the ionospheric TEC modeling.

Then, the slant ionospheric delay can be, respectively, expressed as:

$$\text{STEC}_r^s(k) = \begin{cases} \text{MF}(E) \cdot \text{VTEC}_r(\varphi, T), & \text{Single-layer MF} \\ \sum_{i=1}^n \text{MF}(E_i) \cdot \text{VTEC}_r(\varphi_i, T_i), & \text{Multi-layer MF} \end{cases} \quad (21)$$

Hence, the STEC converted from the VTEC with respect to the single-layer and multi-layer MFs are obtained.

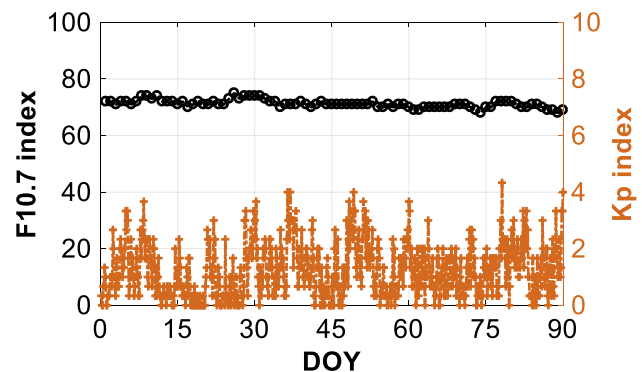


Fig. 3 Solar flux F10.7 and geomagnetic Kp indices during DOY 1-90, 2020

Experimental data and processing strategies

In order to validate the reliability of ionospheric TEC modeling with the multi-layer MF, 74 station datasets collected from the IGS MGEX network during the day of year (DOY) 001-090, 2020 are processed to analyze the performances. Figure 2 depicts the geometrical distribution of the selected MGEX stations. The selected stations cover the global mainland and the BDS3 has a great IPP distribution over the whole globe, whereas the BDS2 IPP is mainly concentrated on the Australia, Asia and Europe areas. The reason is that only 13 BDS2 satellites are available, and 5 of them are geostationary (GEO) satellites. Table 1 provides the information of the selected 74 MGEX stations, including the station name, receiver and antenna types.

Table 2 summarizes the detailed processing strategies for ionospheric VTEC and BDS2/BDS3 satellite DCB retrieval. We comment on some points that deserve special emphasis here. A cutoff angle of 7° is set to rule out the noisy measurements. The forward and backward Kalman filter is

especially applied to alleviate the influence of the inaccuracy of the ionospheric observables in the initial time. In multi-layer MF, the corresponding parameters, including peak height hmF2 and scale height values, are obtained from the external models. The input F10.7 parameters are provided by the Space Environment Prediction Center. The zero-mean condition is utilized to mitigate the impact of rank deficient of BDS satellite DCBs. Figure 3 depicts the variations of the solar flux F10.7 (<http://www.sepc.ac.cn/>) and geomagnetic Kp (<http://isgi.unistra.fr/>) indices during DOY 1-90, 2020, in which we can find that the solar activity conditions are stable and the geomagnetic activity was almost low to moderate ($Kp < 4$). For the layering case, the distance of two consecutive shells is set as 50 km below the 2000 km height and then set as 1000 km up to the 1000 km height.

Fig. 4 Time series of the VTEC estimates retrieved with SFPPP, DFPPP and CCL methods by two MFs for a pair of the collocated stations ZIM2 (top) and ZIM3 (bottom) on 3 days

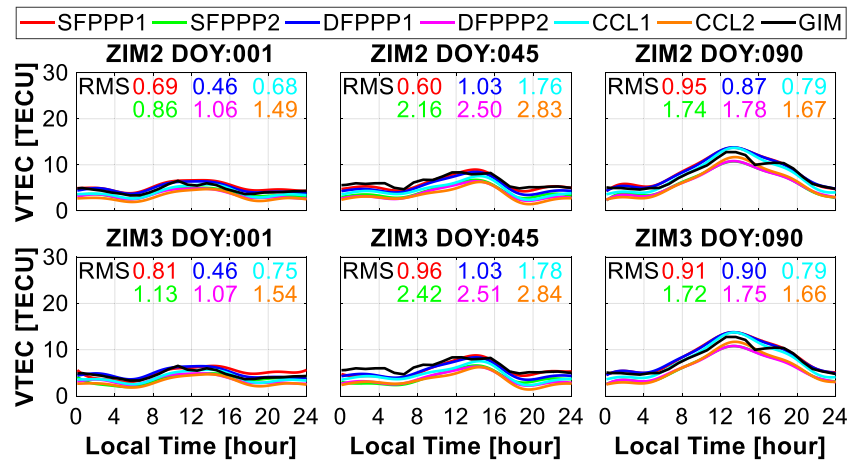
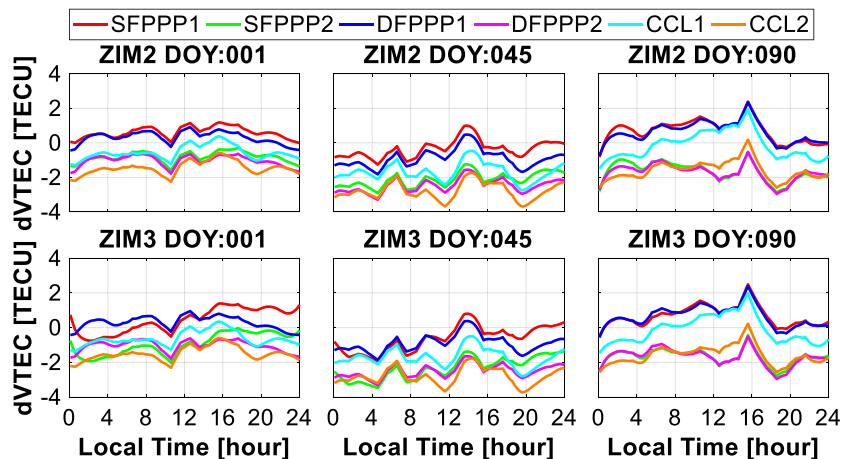


Fig. 5 Time series of the VTEC difference between the estimated values and GIM values retrieved with SFPPP, DFPPP and CCL methods by two MFs for stations ZIM2 (top) and ZIM3 (bottom) on 3 days



Performance analysis

The section starts with the validation of the estimated VTEC. Then, the performances of VTEC estimates are analyzed by the BDS IC SFPPP schemes. Finally, we evaluate the stability of the BDS satellite and receiver DCB estimates, which are determined during the VTEC estimation process.

VTEC validation by IGS products

To validate the reliability and accuracy of the derived ionospheric VTEC values, we analyzed the VTEC estimates derived from SFPPP, DFPPP and CCL approaches implemented with the single-layer and multi-layer MFs. In particular, the single-frequency approach is based on the BDS BII data. As an example, Fig. 4 depicts the time series of the VTEC estimates with 5-min time resolution retrieved with SFPPP, DFPPP and CCL approaches by two MFs for a pair of the collocated stations ZIM2 and ZIM3 on DOY 001, 045 and 090. Different subplots denote the VTEC estimates of the two stations on different days. The VTEC estimates with different approaches are represented by different colors. The VTEC for the receiver zenith IPPs is considered equal for the two collocated stations. Both two stations are

located in the midlatitude area in the northern hemisphere. The IGS global ionospheric map (GIM) VTEC values are used as the reference to evaluate the VTEC accuracy and also depicted in the figure, whose accuracy is 2–8 TEC unit (TECU) (Hernández-Pajares et al. 2009). The VTEC time series reveal the VTEC diurnal variation of the stations, in which the maximum values are near the local noon (14:00) and the minimum values are near the local night (00:00). It is apparent that the time series of the SFPPP, DFPPP and CCL with the two MFs have similar trends with the GIM VTEC values. Figure 5 shows the time series of the VTEC differences between the estimated values and GIM values with SFPPP, DFPPP and CCL approaches by two MFs for stations to better emerge the features in the different strategies ZIM2 and ZIM3 on three days. The root mean square (RMS) of the differences between the models derived VTEC and GIM VTEC reveals that the VTEC extracted methods with the single-layer MF have the better consistency with the IGS GIM values compared to the solutions with the multi-layer MF. It is reasonable that the adopted GIM VTEC values also utilize the single-layer MF that neglects the ionospheric horizontal gradient (Schaer et al. 1996).

Furthermore, Fig. 6 shows the time series of the single-difference VTEC estimates at two stations retrieved with SFPPP, DFPPP and CCL methods with two MFs, as well as

Fig. 6 Time series of the VTEC estimate differences retrieved with SFPPP, DFPPP and CCL methods by two MFs for the stations ZIM2 and ZIM3 on 3 days

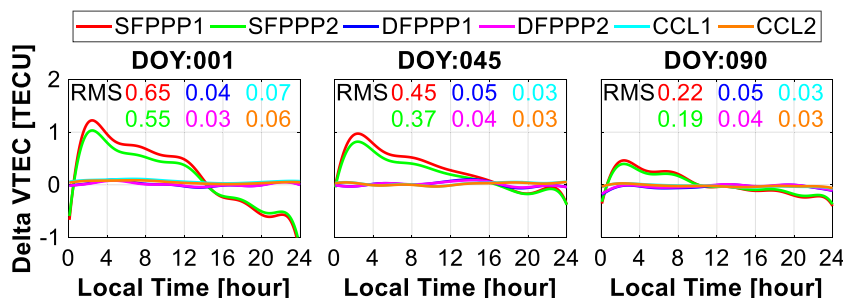


Fig. 7 Time series of the VTEC estimates for the random stations ABMF, HUEG, MRO1, POTS, SOLO and UNSA retrieved with SFPPP, DFPPP and CCL methods

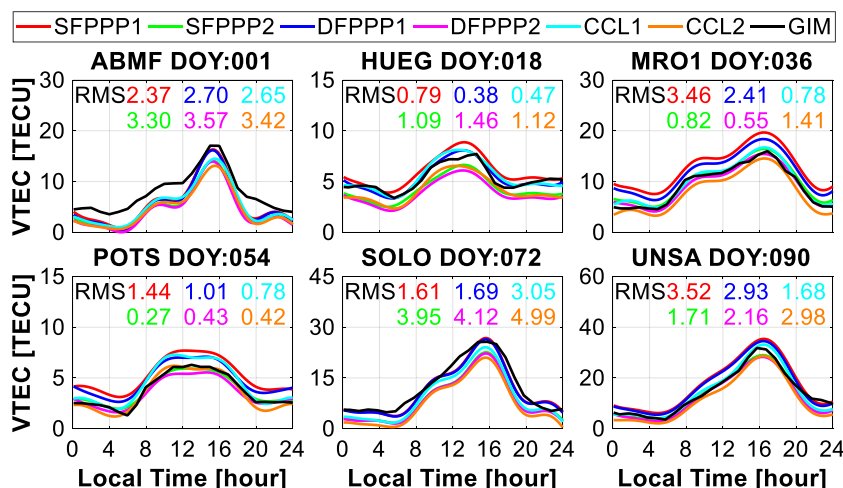


Fig. 8 Distribution of the RMS, mean bias and STD of the VTEC estimated differences derived by the SFPPP, DFPPP and CCL methods with two MFs compared with the IGS products, in which (a, b) denotes the corresponding median and mean values

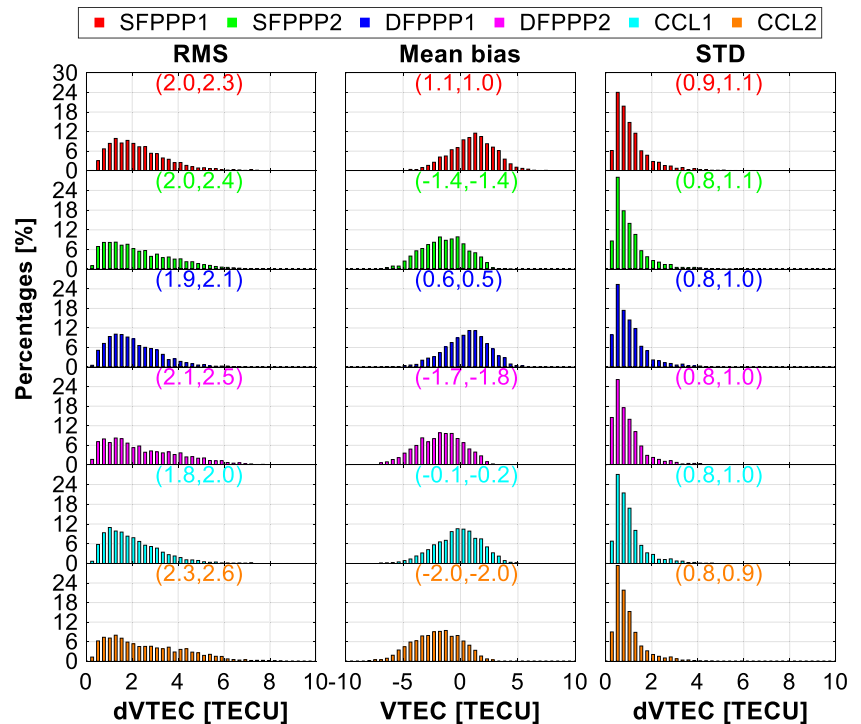
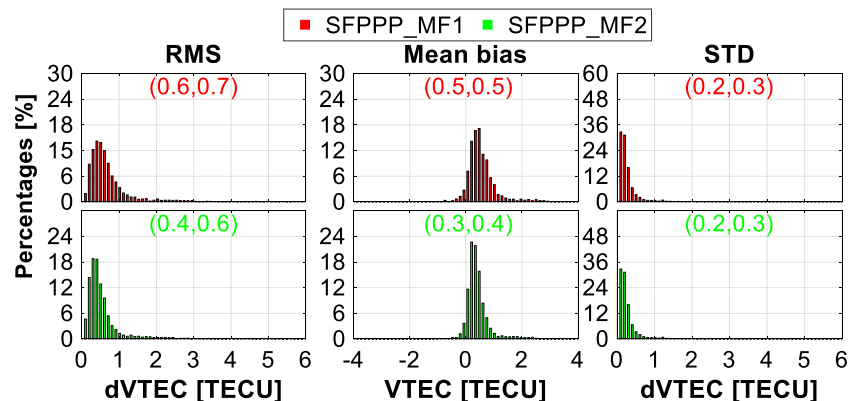


Fig. 9 Distribution of the RMS, mean bias and STD of the VTEC estimated differences derived by the SFPPP with two MFs compared with the VTEC estimates by the DFPPP method using the corresponding MF



the RMS of the single-difference VTEC estimates. The single-difference values of the VTEC estimates can reflect the VTEC precision of the methods. The single differences of the VTEC estimates at different days have remarkable similarities and the precision of VTEC estimates for DFPPP and CCL methods is better than the SFPPP solutions. By comparing with the single-difference VTEC values, we can find that the multi-layer MF utilization can improve the precision of the VTEC estimates, especially for the SFPPP solutions.

Now turn to Fig. 7, in which each panel depicts the time series of the VTEC estimates for six stations ABMF, HUEG, MRO1, POTS, SOLO and UNSA on one random day. We only present the results of the six random stations here though we have got plenty of the results. We can see that the ionospheric VTEC estimates obtained by the SFPPP, DFPPP

and CCL approaches have an accuracy of few TECUs when using the GIM VTEC values as the reference. The SFPPP solutions with single-layer and multi-layer MFs can estimate the VTEC with the general reliability and convenience.

Figure 8 describes the RMS distribution, mean bias and standard deviation (STD) of the VTEC estimate differences derived by the SFPPP, DFPPP and CCL methods by the single-layer and multi-layer MFs with respect to the IGS GIM products. The corresponding median and mean values are also summarized. The internally calculated STD of the VTEC estimates denotes the formal precision. It is apparent that the estimated VTEC accuracy by the different method is approximately 2 TECU using the GIM as the reference. In accordance with our expectation, the VTEC estimates with the CCL method by single-layer MF have the

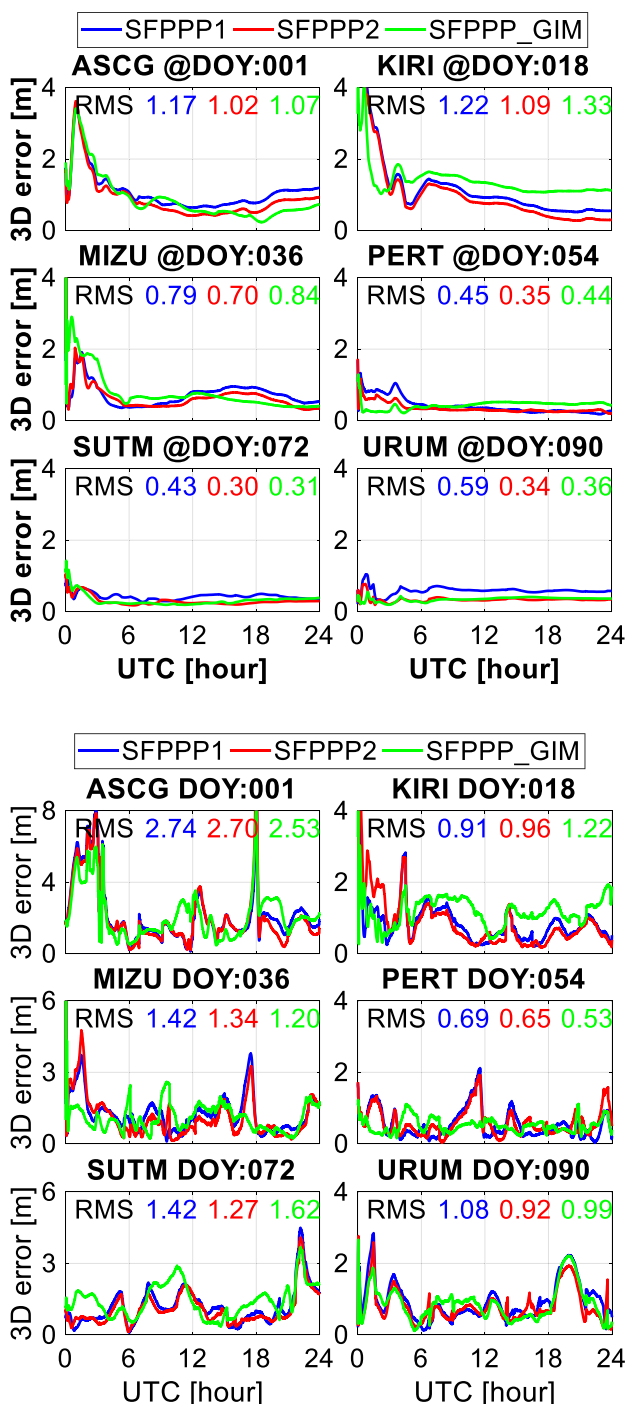


Fig. 10 3D static (top) and kinematic (bottom) positioning error of the stations ASCG, KIRI, MIZU, PERT, SUTM and URUM by IC SFPPP with the ionospheric correction from the SFPPP solutions with the single-layer and multi-layer MFs and IGS GIM products

best consistency with IGS GIM for applying the same slant ionospheric delay extraction and MF methods (Jee et al. 2010). Compared with the different methods with single-layer MF, the VTEC estimates have the systematical bias of 1–2 TECU when applying the multi-layer MF. On the whole,

the estimated VTEC values by the multi-layer MF are generally less than estimated values by the single-layer MF. The STD of VTEC estimates with the two MFs has no obvious differences for the CCL, SFPPP and DFPPP solutions.

To further quantify and analyze the VTEC estimate performances by the SFPPP schemes, we calculated the RMS, mean bias and STD for two SFPPP-derived time series by using the corresponding DFPPP-derived time series with the same MF and present the distribution of results in Fig. 9. When using the corresponding DFPPP-derived VTEC values as the references, the accuracy of the SFPPP-derived VTEC estimates with multi-layer MF is improved compared with the solution with the single-layer MF. For instance, the mean RMS of VTEC differences with the multi-layer MF is reduced by 33.3% compared with the single-layer MF values. In other words, the SFPPP and DFPPP zenith VTEC estimates are closer to each other under the scenarios of multi-layer MF.

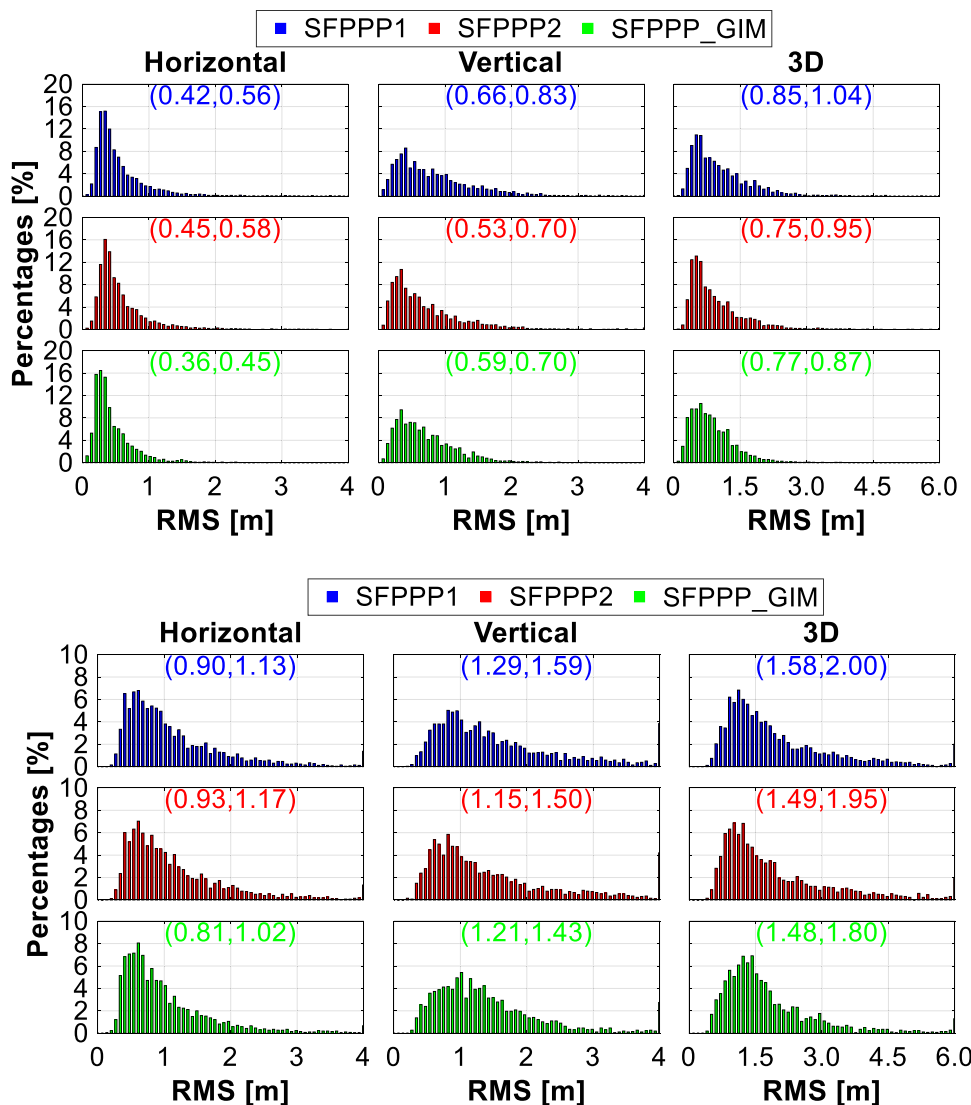
VTEC assessment by SFPPP

The ionospheric delay modelling is relatively complicated in SFPPP. For the purpose of the elimination of the rank deficiency and enhancement of the model, the ionosphere-weighted (IW) model is established with a prior ionospheric constraint from the external models. With the assistance of the external ionospheric model, the IC model is built. The performance is sensitive to the inaccuracy of external ionospheric information and can thus be used as an indicator to analyze the VTEC estimate performances.

To further verify the accuracy and reliability of the VTEC estimates by SFPPP, we conduct the BDS IC SFPPP solutions in both static and kinematic scenarios with the ionospheric correction derived by SFPPP with single-layer and multi-layer MFs, as well as the GIM. For each station, the ionosphere-corrected values are obtained from each station and only adopt to itself. Figure 10 depicts the 3D positioning error of the six random selected stations by the BDS IC SFPPP. Obviously, 3D positioning performances of IC SFPPP for the selected stations with the multi-layer MF SFPPP-derived ionospheric correction are better when compared to the solutions with the single-layer MF in both static and kinematic cases because the multi-layer MF supposedly mitigates errors due to considering the large ionosphere horizontal gradient. In most cases for the six stations, the positioning performances of IC SFPPP implemented with GIM ionospheric correction are better than the solutions with single-layer MF approaches but worse than the multi-layer MF approaches.

Figure 11 depicts the RMS distribution of the horizontal, vertical and 3D positioning error from the BDS IC SFPPP with the ionospheric correction from the SFPPP solutions with two MFs and IGS GIM products. Moreover, the 90-day

Fig. 11 Distribution of the RMS of the horizontal, vertical and 3D positioning error of the BDS IC SFPPP with the ionospheric correction from the SFPPP solutions with two MFs and IGS GIM products for static (top) and kinematic (bottom) solutions



mean positioning errors of the BDS static and kinematic IC SFPPP by three schemes are shown in Fig. 12. The positioning performances of the BDS IC SFPPP utilizing the ionospheric correction provided by multi-layer MF-derived values are better. For example, the mean positioning accuracy of the BDS IC SFPPP utilizing the multi-layer MF-derived values is improved by 11.8% and 5.7%, in static and kinematic scenarios, respectively, compared with the solutions utilizing the single-layer MF-derived values. The positioning performances of the BDS IC SFPPP with the ionospheric corrections by multi-layer MF-derived values and GIM values are at a much closer level. For example, the median positioning accuracy of the BDS IC SFPPP with two schemes are (0.75, 0.77) and (1.49, 1.48) m in static and kinematic scenarios, respectively. On the other hand, the positioning performances of stations located at low latitude areas are worse than the stations located in the mid- and high-latitude areas. The phenomena are reasonable for the

ionospheric delays at the low latitude areas are more active than other areas. The applied GTSF function cannot fully reflect the ionospheric variations in the low latitude areas. Overall, the positioning accuracy of the stations in Australia, Asia and Europe areas is higher than other places due to the more observed BDS satellites.

BDS DCB validation

The satellite DCB and VTEC estimates have the strong correlation in ionospheric VTEC modeling. Let us first pay our attention on the satellite DCB daily estimates by the SFPPP approaches. The B1I/B3I signals are simultaneously observed by the BDS2 and BDS3 satellites. This study mainly focuses on the analysis of BDS C2I-C6I DCB for the B1I/B3I signals by the SFPPP schemes with two MFs. Figure 13 shows the time series of BDS (BDS2+BDS3) satellite DCB daily estimates during the period DOY 001-090

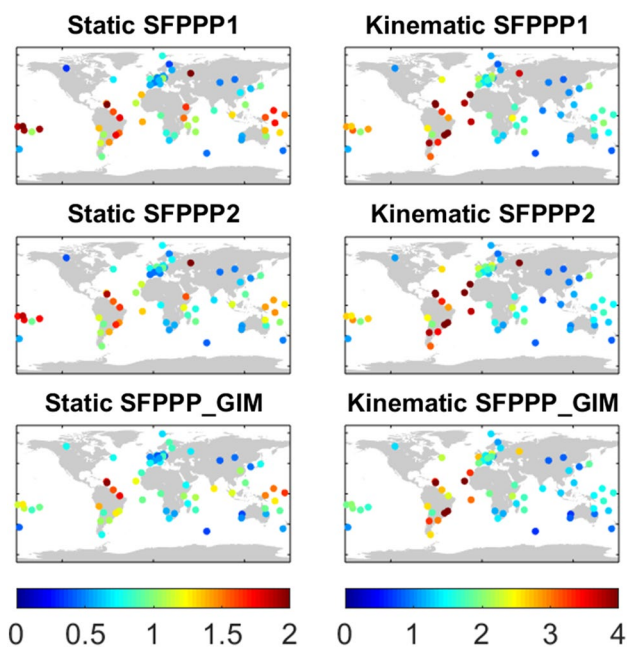
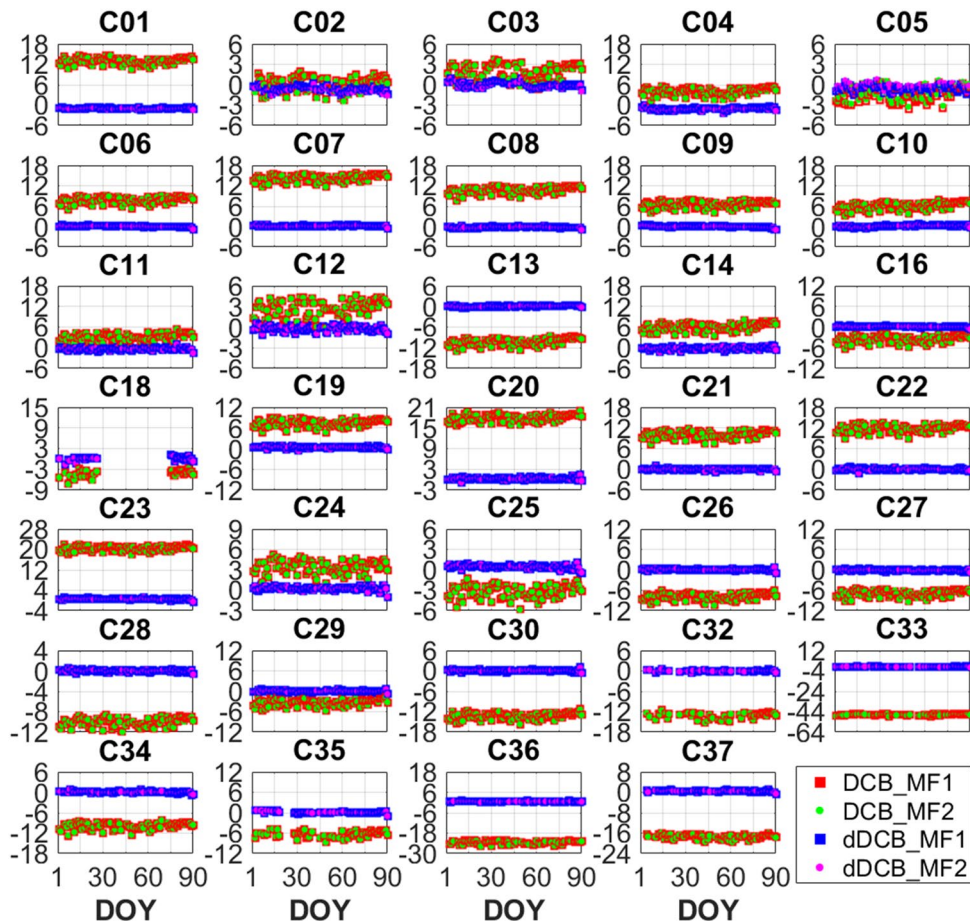


Fig. 12 90-day mean positioning error of the static and kinematic PPP using the ionospheric corrections by two MFs and GIM

by the SFPPP solution with two MFs and their differences with respect to the DCB products from CAS (Chinese Academy of Sciences) for a representative station GAMG. It is worth noting that the zero-mean conditions for the DCBs of SFPPP solutions and CAS products are different for the observations with different satellites are applied. Hence, the satellite and receiver DCBs need to be corrected by transforming estimated values to the same zero-mean condition. The corrected method of satellite and receiver DCBs refer to Jin et al. (2016). The estimated BDS DCBs vary between the -46.0 and 22.0 ns. On partial days, nothing can be observed for some satellites, such as the BDS C18 satellites on DOY 028-072, 2020. The daily BDS DCB estimates appear to be stable, and the satellite DCB values by the SFPPP method with single-layer and multi-layers MFs are overlapped and very closed. To further evaluate the accuracy of the estimated DCB, Fig. 14 depicts the time series of the RMS of the DCB differences with respect to the CAS products by the SFPPP method with single-layer and multi-layers MFs at stations MAGY, MRO1, NNOR and PNGM. The RMS of DCB differences for all observed BDS satellites is also shown in the figure. It is apparent that DCB accuracy is hardly affected by the different MFs for the SFPPP method.

Fig. 13 DCB time series (unit: ns) of BDS C2I-C6I DCBs during the period DOY 001-090, 2020 by the SFPPP method at the station GAMG. The differences with respect to CAS products are also shown



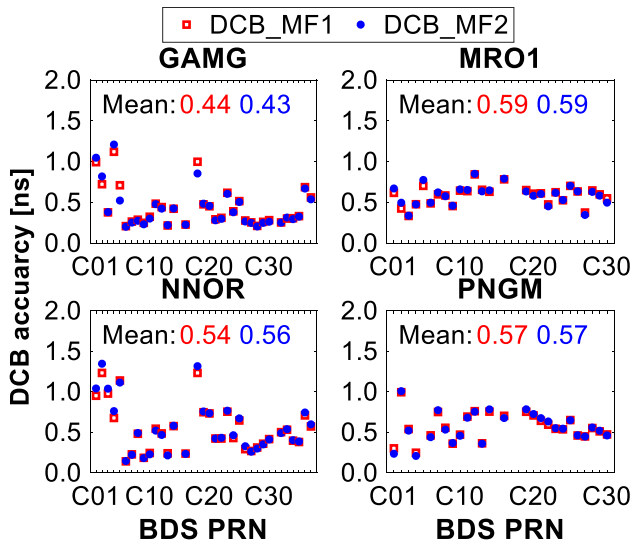
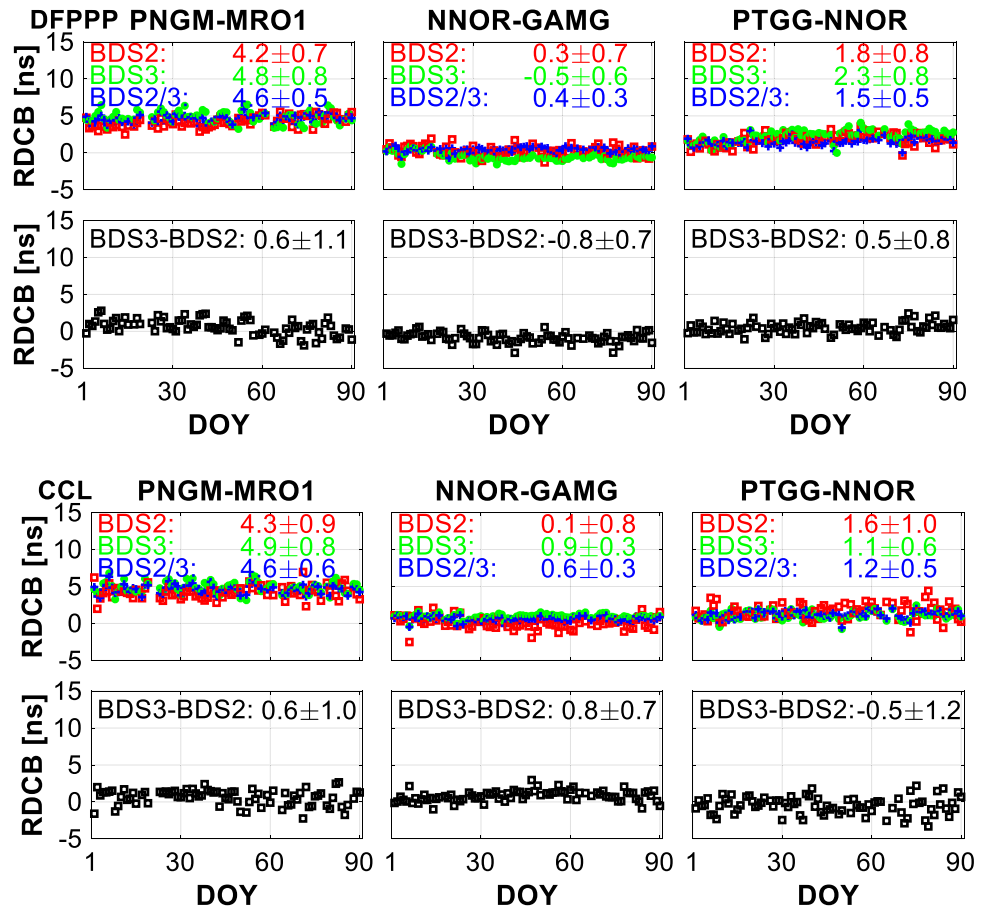


Fig. 14 Time series of RMS for the BDS C21-C61 receiver DCB differences with respect to the CAS products during the period DOY 001-090, 2020

The estimated satellite DCBs are reliable when compared with the CAS DCB products.

To verify the existence of the systematical bias between the BDS2 and BDS3 receiver DCB, we estimate the receiver DCB by the DFPPP and CCL solutions with the multi-layer MF. The receiver DCB values by two MFs are consistent, and thus, we neglect the receiver DCB by the single-layer MF. The SFPPP method is not considered for the estimated receiver-dependent parameter to encompass only the receiver clock offsets on the first epoch on different days. The BDS2-only, BDS3-only and BDS2/BDS3 solutions are conducted, respectively, for the DFPPP and CCL schemes with the multi-layer MF. The different zero-mean conditions for three solutions are adopted to solve the rank deficiency of the normal equation matrix. The biases exist between the BDS2-only, BDS3-only and BDS2/BDS3 solutions with the specific zero-mean conditions. Thus, an additional station with the same observed satellites is set as the reference to subtract the biases of the corresponding DCB values. In fact, the operation denotes the single difference between stations of the receiver DCBs with the same satellite types. Figure 15 depicts the time series of the single-difference receiver DCBs with respect to one reference station by the BDS2-only, BDS3-only and BDS2/BDS3 DFPPP and CCL solutions during the period DOY 001-090, 2020. The BDS2 and BDS3 receiver DCB differences are also shown in the figure.

Fig. 15 Time series of the single-difference receiver DCBs with respect to one reference station by the BDS2-only, BDS3-only and BDS2/BDS3 DFPPP (top) and CCL (bottom) solutions during the period DOY 001-090, 2020. The double differences between the BDS2 and BDS3 are also shown



The double difference is provided to analyze the BDS2 and BDS3 DCB differences. We can see that the mean BDS2 and BDS3 DCB differences are close to zero, whose values are less than the corresponding precisions. The systematic bias of the BDS2/BDS3 receiver DCB is less than 0.8 ns (approximately 0.2 m), which has a minor impact on the GNSS pseudorange-based positioning performances. Furthermore, the STDs of the BDS2/BDS3 receiver DCBs are smaller than the BDS2-only or BDS3-only solutions for the selected three-pair stations, which indicates that the stability of receiver DCB is better when combining the BDS2 and BDS3 observations. Hence, it is recommended to estimate the satellite and receiver DCB values by considering the BDS2 and BDS3 as a whole system during the ionospheric VTEC modeling.

Conclusion

To overcome deficiencies that the customarily used single-layer MF ignores the horizontal gradients and vertical ionosphere structures, this study proposed the SFPPP method to retrieve the ionospheric VTEC and satellite DCBs with the newly deployed BDS satellites based on the multi-layer MF. The corresponding dual-frequency methods, including the CCL and DFPPP with the single-layer and multi-layer MFs are also conducted. Seventy-four MGEX stations during the 90 days are utilized to validate the performances of ionospheric VTEC modeling with the multi-layer MF. The main results are obtained as follows:

- (1) The estimated VTEC precision by the DFPPP and CCL is better than the SFPPP solutions. By substituting the multi-layer MF for single-layer MF, the VTEC precision is improved, especially for the SFPPP solutions. For instance, using the DFPPP-derived VTEC as the reference, the median RMS VTEC error decreases from 0.6 to 0.4 TECU. The estimated VTEC accuracy by the SFPPP, DFPPP and CCL is approximately 2 TECU when using the GIM as the reference.
- (2) The positioning errors of IC SFPPP with the multi-layer MF SFPPP-derived ionospheric correction perform better than the single-layer MF solutions in both static and kinematic situations. The positioning of stations located at low latitude areas is worse than at the mid- and high-latitude areas because of the more active ionospheric delays. The positioning of stations in Australia, Asia and Europe is better when more BDS satellites are available.
- (3) The estimated BDS DCB with high accuracy in the SFPPP has no significant difference with the different MFs. The BDS2 and BDS3 receiver DCBs have no

significant systematical bias in the ionospheric VTEC modeling processing.

In this study, the SFPPP with multi-layer MF is demonstrated as a promising and reliable method to retrieve the VTEC. The refined SFPPP method is more attractive for low-cost receivers and can monitor the ionospheric delay using only single-frequency BDS pseudorange and carrier phase observations.

Acknowledgements This work was supported by the National Natural Science Foundation of China Project (Grant No. 12073012), National Natural Science Foundation of China-German Science Foundation Project (Grant No. 41761134092) and Shanghai Leading Talent Project (Grant No. E056061). The authors acknowledge the IGS, MGEX, GFZ and CAS and provide the BDS observation data, BDS precise orbit and clock and DCB products.

Data availability The BDS observation data from MGEX networks are available at cddis.gsfc.nasa.gov/pub/gps/data/. The BDS precise orbit and clock products from GFZ are available at <http://www.gfz-potsdam.de/GNSS/products/mgex/>. The GIM products are provided from the <http://www.cddis.gsfc.nasa.gov/pub/gps/products/ionex/>. The BDS DCBs are provided at the <http://www.cddis.gsfc.nasa.gov/pub/gps/products/mgex/dcb/>. The applied solar flux F10.7 is obtained from the <http://www.sepc.ac.cn>.

References

- Brunini C, Azpilicueta F (2010) GPS slant total electron content accuracy using the single layer model under different geomagnetic regions and ionospheric conditions. *J Geod* 84(5):293–304
- Chen L, Yi W, Song W, Shi C, Lou Y, Cao C (2018) Evaluation of three ionospheric delay computation methods for ground-based GNSS receivers. *GPS Solut* 22:125
- Ciraolo L, Azpilicueta F, Brunini C, Meza A, Radicella S (2007) Calibration errors on experimental slant total electron content (TEC) determined with GPS. *J Geod* 81:111–120
- dos Santos Prol F, de Oliveira Camargo P, Monico JFG, Mueller MTD (2018) Assessment of a TEC calibration procedure by single-frequency PPP. *GPS Solut* 22:35
- Gao Z, Ge M, Shen W, Zhang H, Niu X (2017) Ionospheric and receiver DCB-constrained multi-GNSS single-frequency PPP integrated with MEMS inertial measurements. *J Geod* 91:1351–1366
- Hernández-Pajares M, Juan J, Sanz J, García-Fernández M (2005) Towards a more realistic ionospheric mapping function. XXVIII URSI General Assembly, Delhi
- Hernández-Pajares M, Juan J, Sanz J, Orus R, Garcia-Rigo A, Feltens J, Komjathy A, Schaer S, Krankowski A (2009) The IGS VTEC maps: a reliable source of ionospheric information since 1998. *J Geod* 83(3):263–275. <https://doi.org/10.1007/s00190-008-0266-1>
- Hoque MM, Jakowski N (2011) A new global empirical NmF2 model for operational use in radio systems. *Radio Sci* 46:1–13
- Hoque M, Jakowski N (2012) A new global model for the ionospheric F2 peak height for radio wave propagation. *Ann Geophys* 30(5):797–809
- Hoque MM, Jakowski N (2013) Mitigation of ionospheric mapping function error. In: Proceedings of ION GNSS + 2013, Institute of Navigation, Nashville, Tennessee, USA, September 16–20, pp 1848–1855

- Hoque M, Jakowski N (2015) An alternative ionospheric correction model for global navigation satellite systems. *J Geod* 89:391–406
- Jakowski N, Hoque M, Mayer C (2011) A new global TEC model for estimating transionospheric radio wave propagation errors. *J Geod* 85:965–974
- Jee G, Lee HB, Kim YH, Chung JK, Cho J (2010) Assessment of GPS global ionosphere maps (GIM) by comparison between CODE GIM and TOPEX/Jason TEC data: Ionospheric perspective. *J Geophys Res Space Phys* 115(A10):A10319
- Jiang H, Wang Z, An J, Liu J, Wang N, Li H (2018) Influence of spatial gradients on ionospheric mapping using thin layer models. *GPS Solut* 22:2
- Jin S, Su K (2020) PPP models and performances from single-to quad-frequency BDS observations. *Satell Navig* 1:1–13
- Jin R, Jin S, Feng G (2012) M_DCB: Matlab code for estimating GNSS satellite and receiver differential code biases. *GPS Solut* 16:541–548
- Jin S, Jin R, Li D (2016) Assessment of BeiDou differential code bias variations from multi-GNSS network observations. *Ann Geophys* 09927689:34
- Klobuchar JA (1987) Ionospheric time-delay algorithm for single-frequency GPS users. *IEEE Trans Aerosp Electron Syst* 23:325–331
- Komjathy A, Sparks L, Mannucci AJ, Coster A (2005) The ionospheric impact of the October 2003 storm event on wide area augmentation system. *GPS Solut* 9:41–50
- Kong J, Yao Y, Liu L, Zhai C, Wang Z (2016) A new computerized ionosphere tomography model using the mapping function and an application to the study of seismic-ionosphere disturbance. *J Geod* 90:741–755
- Kouba J (2009) A guide to using International GNSS Service (IGS) products. IGS Central Bureau, Jet Propulsion Laboratory, Pasadena, p 34
- Landskron D, Böhm J (2018) VMF3/GPT3: refined discrete and empirical troposphere mapping functions. *J Geod* 92:349–360
- Leick A, Rapoport L, Tatarski D (2015) GPS satellite surveying. Wiley, New York
- Li Z, Yuan Y, Wang N, Hernandez-Pajares M, Huo X (2015) SHPTS: towards a new method for generating precise global ionospheric TEC map based on spherical harmonic and generalized trigonometric series functions. *J Geod* 89:331–345
- Li M, Yuan Y, Zhang B, Wang N, Li Z, Liu X, Zhang X (2018) Determination of the optimized single-layer ionospheric height for electron content measurements over China. *J Geod* 92:169–183
- Li M, Zhang B, Yuan Y, Zhao C (2019a) Single-frequency precise point positioning (PPP) for retrieving ionospheric TEC from BDS B1 data. *GPS Solut* 23:18
- Li Z, Wang N, Wang L, Liu A, Yuan H, Zhang K (2019b) Regional ionospheric TEC modeling based on a two-layer spherical harmonic approximation for real-time single-frequency PPP. *J Geod* 93:1659–1671
- Li Z et al (2020) IGS real-time service for global ionospheric total electron content modeling. *J Geod* 94:1–16
- Liu T, Zhang B, Yuan Y, Li M (2018) Real-time precise point positioning (RTPPP) with raw observations and its application in real-time regional ionospheric VTEC modeling. *J Geod* 92:1267–1283
- Liu T, Zhang B, Yuan Y, Zhang X (2020) On the application of the raw-observation-based PPP to global ionosphere VTEC modeling: an advantage demonstration in the multi-frequency and multi-GNSS context. *J Geod* 94:1–20
- Nava B, Coisson P, Radicella S (2008) A new version of the NeQuick ionosphere electron density model. *J Atmos Sol Terr Phys* 70:1856–1862
- Petit G, Luzum B (eds) (2010) IERS Conventions (2010), IERS Technical Note 36. Verlag des Bundesamts für Kartographie und Geodäsie, Frankfurt am Main, Berlin
- Psychas D, Verhagen S, Liu X, Memarzadeh Y, Visser H (2018) Assessment of ionospheric corrections for PPP-RTK using regional ionosphere modelling. *Meas Sci Technol* 30:014001
- Ren X, Zhang X, Xie W, Zhang K, Yuan Y, Li X (2016) Global ionospheric modelling using multi-GNSS: BeiDou, Galileo GLO-NASS and GPS. *Sci Rep* 6:33499
- Rishbeth H, Garriott OK (1969) Introduction to ionospheric physics. Academic Press, New York, p 331
- Schaer S, Beutler G, Rothacher M, Springer TA (1996) Daily global ionosphere maps based on GPS carrier phase data routinely produced by the CODE Analysis Center. In: Proceedings of the IGS AC workshop, Silver Spring, pp 181–192
- Schüler T, Oladipo OA (2014) Single-frequency single-site VTEC retrieval using the NeQuick2 ray tracer for obliquity factor determination. *GPS Solut* 18:115–122
- Sterle O, Stopar B, Prešeren PP (2015) Single-frequency precise point positioning: an analytical approach. *J Geod* 89:793–810
- Su K, Jin S (2018) Improvement of multi-GNSS precise point positioning performances with real meteorological data. *J Navig* 71:1363–1380
- Su K, Jin S (2019) Triple-frequency carrier phase precise time and frequency transfer models for BDS-3. *GPS Solut* 23:86
- Su K, Jin S, Hoque M (2019) Evaluation of ionospheric delay effects on multi-GNSS positioning performance. *Remote Sens* 11:171
- Tu R, Zhang H, Ge M, Huang G (2013) A real-time ionospheric model based on GNSS precise point positioning. *Adv Space Res* 52:1125–1134
- Wu JT, Wu SC, Hajj GA, Bertiger WI, Lichten SM (1992) Effects of antenna orientation on GPS carrier phase. *Astrodynamic* 18:1647–1660. (**Astrodynamic** 1991)
- Xiang Y, Gao Y (2019) An enhanced mapping function with ionospheric varying height. *Remote Sens* 11:1497
- Yuan Y, Wang N, Li Z, Huo X (2019) The BeiDou global broadcast ionospheric delay correction model (BDGIM) and its preliminary performance evaluation results. *Navigation* 66:55–69
- Yuan L, Jin S, Hoque M (2020) Estimation of LEO-GPS receiver differential code bias based on inequality constrained least square and multi-layer mapping function. *GPS Solut* 24:1–12
- Zhang B, Ou J, Yuan Y, Li Z (2012) Extraction of line-of-sight ionospheric observables from GPS data using precise point positioning. *Sci China Earth Sci* 55:1919–1928
- Zhang B, Teunissen PJ, Yuan Y, Zhang H, Li M (2018) Joint estimation of vertical total electron content (VTEC) and satellite differential code biases (SDCBs) using low-cost receivers. *J Geod* 92:401–413
- Zhang B, Teunissen PJ, Yuan Y, Zhang X, Li M (2019) A modified carrier-to-code leveling method for retrieving ionospheric observables and detecting short-term temporal variability of receiver differential code biases. *J Geod* 93:19–28

Publisher's Note Springer Nature remains neutral with regard to jurisdictional claims in published maps and institutional affiliations.



Ke Su is currently a Ph.D candidate at the Shanghai Astronomical Observatory, Chinese Academy of Sciences, Shanghai, China. His research interests include GNSS ionosphere and PPP applications.



Shuanggen Jin is a Professor and Group Head at the Shanghai Astronomical Observatory, CAS, Shanghai, China. His main research areas include satellite navigation, space geodesy, remote sensing and space/planetary exploration. He has published over 500 papers in peer-reviewed journals and proceedings. He has received 100-Talent Program of CAS, Fellow of IAG, Fellow of IUGG, Member of Academia Europaea, Member of Russian Academy of Natural Sciences, Mem-

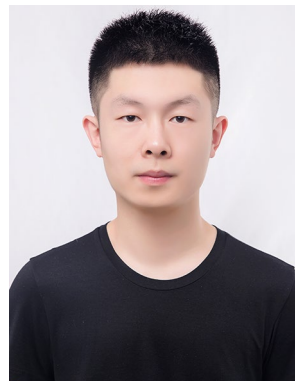
ber of European Academy of Sciences and Member of Turkish Academy of Sciences.



J. Jiang is currently a B.Sc candidate at Nanjing University of Information Science and Technology, Nanjing, China. His area of research is currently multi-GNSS PPP.



Mainul Hoque received his bachelor's degree in electrical and electronics engineering in 2000 and was awarded a Ph.D. in 2009 from the University of Siegen, Germany. He has been working on ionospheric modeling, including higher-order propagation effects at the German Aerospace Center since 2004. He was involved in several national, ESA and EU projects related to ionospheric research.



Liangliang Yuan received a Ph.D. degree at the Shanghai Astronomical Observatory, Chinese Academy of Sciences, Shanghai, China. His research interests include thermosphere-ionosphere coupling and GNSS ionospheric radio occultation.